

Performance Study of the IceCube Upgrade Camera System

The IceCube Collaboration

(a complete list of authors can be found at the end of the proceedings)

E-mail: rott@physics.utah.edu, pmj0324@g.skku.edu,
karl.jansson@uclouvain.be, u1335412@utah.edu, seo.won.choi@utah.edu

The IceCube Upgrade Camera System is a novel calibration system designed to calibrate the IceCube detector by measuring the optical properties of the Antarctic ice. The system comprises nearly 2,000 cameras and illumination LEDs, which are present on every D-Egg and mDOM—the newly designed optical modules for the IceCube Upgrade. These units, deployed across the IceCube Upgrade volume, will capture transmission and reflection images that can be used to characterize the optical properties of both the refrozen ice within drill holes and the bulk ice between strings. Additionally, the images can aid in determining the positions of the optical modules the camera systems are mounted on. To maximize the system's performance, various image analysis methodologies have been explored, ranging from classical maximum likelihood estimation to AI-based approaches using neural networks. In this study, we present preliminary results on the performance of these methods based on images generated by a simulation tool developed specifically for this system.

Corresponding authors: Carsten Rott^{1*}, Minje Park², Matti Jansson³, Garrett Iverson¹, Seowon Choi¹

¹ *University of Utah*

² *Sungkyunkwan University*

³ *Université catholique de Louvain*

* Presenter

39th International Cosmic Ray Conference (ICRC2025)
15–24 July 2025
Geneva, Switzerland



1. Introduction

The IceCube Neutrino Observatory [1], located at the geographic South Pole, is a cubic-kilometer-scale detector instrumented with 5,160 digital optical modules (DOMs) arranged on 86 vertical strings between depths of 1.5 km and 2.5 km in the Antarctic ice. The IceCube Upgrade [2] will consist of seven additional strings, numbered 87 to 93, at the center of the existing array. These strings will carry newly designed optical modules, arranged in a denser configuration. While one of the primary goals of the Upgrade is to enhance sensitivity to lower-energy neutrinos, another major objective is to calibrate the IceCube detector. In particular, limited knowledge about the optical properties of the Antarctic ice, which serves as a Cherenkov detection medium, is the source of uncertainty in neutrino event reconstruction [2]. To better constrain these uncertainties, the IceCube Upgrade has added new calibration systems to complement and extend the well-established flasher-based calibration.

The IceCube Upgrade Camera System [3] is a set of such devices composed of wide field-of-view cameras and illumination LEDs. Each of the newly designed optical modules, the D-Eggs [4] and mDOMs [5], is equipped with this system, resulting in nearly 2,000 cameras and LEDs deployed throughout the Upgrade volume. Depending on the combination of the camera and the LED used, the captured images aim to characterize either the bulk ice between strings or the refrozen ice within the drill hole. In addition, the images can aid in refining the positions and orientations of the optical modules they are mounted on.

2. Upgrade Camera System

The camera module utilizes a CMOS color image sensor manufactured by Sony (model IMX225LQR-C), which provides a full resolution of 1312×993 . It is equipped with a fisheye lens that has an approximately 170° field of view in the air. Considering the refractive index of ice and the support structure of the optical modules, their expected field of view after being deployed in the ice is 120° and 90° for D-Egg and mDOM cameras, respectively. The illumination module employs a 451 nm wavelength LED with a beam that has a full width at half maximum (FWHM) of approximately 90° . Both are engineered to operate at temperatures as low as -40°C .

In the D-Egg module, three camera-LED pairs are mounted azimuthally in a horizontal ring around the lower PMT, spaced 120° apart. The cameras are installed on sliding ring segments that allow for slight movement to accommodate compression of the module. After freeze-in, this compression can cause the angular separation between pairs to deviate by up to 12° . In the mDOM, two camera-LED pairs are installed at 45° angles in the upper hemisphere, and one at the bottom facing downward. An additional upward-facing LED is mounted at the top. The D-Egg's camera system configuration supports inter-string imaging, using LEDs and cameras on different strings. While the mDOM's design enables imaging within individual drill holes, using a downward-facing camera with either its adjacent LED or the top LED of the mDOM positioned below.

To develop an analysis framework for measuring ice properties from camera images, we built a dedicated simulation framework, CamSim [6]. (See Figure 1) CamSim generates synthetic images based on user-defined light sources, media properties, and camera models. The simulation starts by defining three components: the emitter, medium, and surface of interest.

3.1 Deep Learning Model – OPTICUS

Geometry estimation relies on clear visual cues like the relative direction of the LED, whereas optical property estimation involves complex, non-linear patterns that are difficult to describe with hand-crafted features. Deep learning models are well-suited for this task. Convolutional Neural Networks (CNNs) extract subtle, spatially distributed features, while transformer-based architectures like Vision Transformer (ViT) [8] capture global contextual relationships across the image.

To leverage both the local feature extraction of CNNs and the global attention of Vision Transformers, we developed a hybrid model named **OPTICUS** (*Optical Property Transformer for IceCube Upgrade Camera System*). As illustrated in Figure 2, the model first partitions the input image into N patches and projects each into an embedding vector via a convolution projection. Next, a learnable CLS token is appended to the sequence, and for all $N + 1$ tokens (N embedding vectors + class token) positional embeddings are applied to preserve spatial context. These tokens are processed by a stack of L Transformer encoder layers [9]. Each layer (depicted in the right inset of Figure 2) consists of a multi-head self-attention mechanism followed by a position-wise feed-forward network. Both sublayers are equipped with residual connections and layer normalization. Finally, the CLS token, which serves as a global representation of the input image, is then fed into a regression head that outputs a single value representing the optical property.

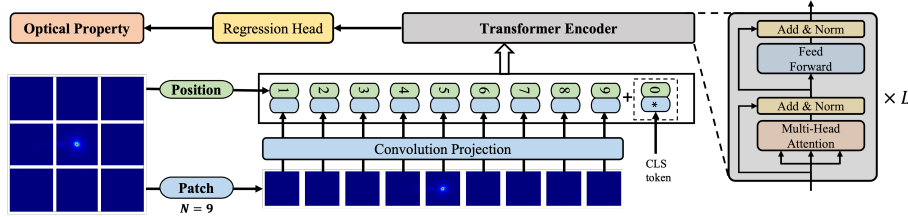


Figure 2: Overall structure of OPTICUS, inspired by the Vision Transformer (ViT) [8]. The input image is split into patches ($N = 9$ shown as an example) and embedded via a convolutional projection. With positional embeddings, the resulting sequence of embedded vectors including CLS token is processed by a stack of L encoder layers. Finally, the CLS token from the last encoder layer is passed through a regression head to predict the optical property.

3.2 Bulk ice model

To develop a model for estimating the bulk ice scattering length, we generated simulated images using a configuration in which a camera from a D-Egg captures light emitted horizontally by an LED from another D-Egg. The two modules are placed 29.8 m apart at the same depth, approximating the inter-string spacing of the IceCube Upgrade. With fixed positions, the camera was rotated in steps of 20° across a range of $\pm 60^\circ$. For each geometric configuration, 10^{12} photons of 470 nm wavelength were injected, while the bulk ice scattering length was varied from 20 m to 100 m in 1 m increments. Based on these 567 simulations, 100 noise realizations were applied to each image, resulting in a total of 56,700 images. Based on this dataset, the **OPTICUS-Bulk** model was configured with $N = 100$ and $L = 5$.

Each image was labeled solely with the bulk ice scattering length, and 90% of the dataset was used for training. The prediction performance of the trained model, **OPTICUS-Bulk**, was evaluated

on the remaining 10%. As shown in Figure 3, the model accurately predicts scattering lengths across the full simulated range. For true scattering lengths of 20 m – 100 m, the average prediction errors are tightly centered around zero, indicating minimal bias. The accuracy is demonstrated with relative error and remains below 0.5% for most cases. The overall 68% containment across the entire range is 0.42%.

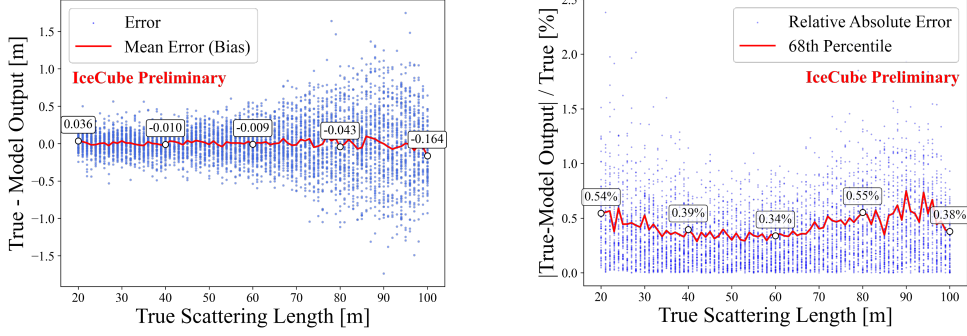


Figure 3: Prediction performance of the **OPTICUS-Bulk** on simulated test data. Prediction bias (left) was assessed using the error defined as true – model output [m]. For each true scattering length, the bias (mean error) was computed, and a few examples are highlighted with circles and text for visual guidance. Prediction accuracy (right) was assessed using the absolute relative error $|true - model\ output|/true[\%]$. For each true scattering length, 68-percentile values are calculated and highlighted with white circles and text. Optical properties other than the bulk ice scattering length are not included.

3.3 Hole ice model

The “hole ice” refers to the refrozen column of ice within each IceCube borehole. A region near its center, known as the “bubble column,” exhibits significantly shorter scattering lengths than the surrounding ice. This column is thought to form primarily from residual air bubbles released during the freezing process, as the hole solidifies inward from the borehole walls.

To develop a model for estimating the bubble column scattering length, we generated simulated images using a configuration in which the downward-facing camera of an upper mDOM observes light emitted by the upward-facing LED of a lower mDOM. Both mDOMs were positioned at the center of the hole ice. The bubble column was modeled at a distance of 10 cm from the center of the hole, with a radius equal to half that of the mDOM. The scattering length of the bubble column was varied from 2 cm to 30 cm in 2 cm steps, resulting in 15 distinct configurations. For each case, five independent simulations were performed to generate base images, and noise was added 200 times per image, yielding a dataset of 15,000 images in total. Based on this dataset, the **OPTICUS-Hole** model was configured with $N = 100$ and $L = 3$.

The prediction performance of the trained model, **OPTICUS-Hole**, is demonstrated in Figure 4. Again, bias is assessed using prediction errors, as shown in the left plot. The errors are tightly centered around zero, indicating that there is no notable bias across the 2–30 cm range. The absolute relative error distribution, shown on the right plot, illustrates the prediction accuracy. The 68% percentile of each bin remains below 2% in all cases, and below 1% across most of the range. The overall 68% containment across the entire range is 0.18%.

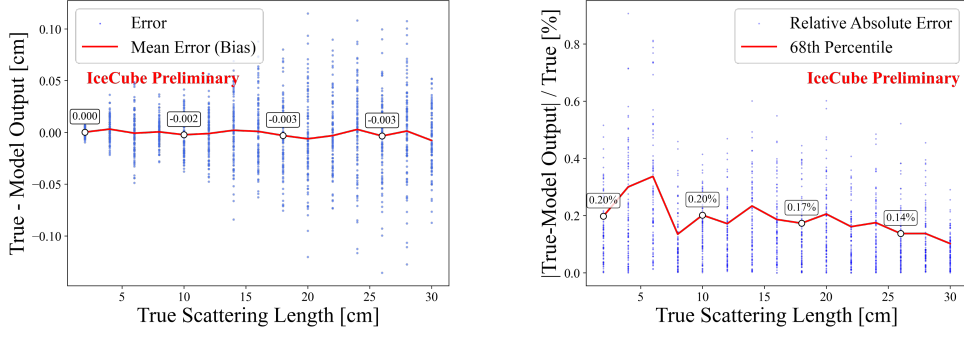


Figure 4: Prediction performance of **OPTICUS-Hole** on simulated test data. Prediction bias (left) and accuracy (right) were assessed in the same manner as for **OPTICUS-Bulk**. For each true scattering length, the 68th percentile of the error distribution was computed, with several examples highlighted with text for visual clarity. Optical properties other than the bubble column scattering length are not included.

Both **OPTICUS-Bulk** and **OPTICUS-Hole** demonstrate percentage-level prediction accuracy. Considering that the simulation was based on a single camera-LED pair, this level of performance suggests strong potential for even greater accuracy when applied to real measurements, where multiple camera-LED combinations will provide redundant and complementary views. Nevertheless, it is important to note that the reported performance reflects statistical uncertainties only, as the validation data was generated under the same simulation configuration as the training data. Other limitations and plans to address them will be discussed in the following section.

4. Geometry Calibration

The positions and directions of the deployed modules affect signal reconstruction as well as calibration measurements using the cameras. Positions will be measured using flashers [10] or where available acoustic modules [11], with orientations measured using in-module accelerometers (tilt) and magnetometers (azimuthal)[12]. Using images that are recorded to measure bulk ice properties, we can get an independent measurement of orientation and using Bayesian inference we can get a refinement of the geometry measurement. To do this we use pictures taken by cameras in 7 D-Eggs at the same depth. As there is a reliable method to obtain the relative depth [13], we only try to constrain the modules' positions in the plane. With the analysis running in layers with one module from each string, we will identify the DOMs with the string numbers.

First, the LED pixels are extracted from camera images. This is done by calculating the center of mass of the pixels with a gradient magnitude within 10% of the highest gradient magnitude in the image. From the LED pixel an angle can be calculated using calibrated projection parameters. Once the angle to two neighboring modules is measured, we add them to get an angle, repeating for all triples of DOMs we get a set of up to 18 angles, which is referred to as the observed angles θ_{obs} .

For each possible configuration of DOM positions, the corresponding angles θ_{cal} can be calculated. Given θ_{cal} and the angle uncertainty σ_{θ} , which is estimated from simulation to be 1° , the likelihood of the observed angles θ_{obs} is given in Equation 1, and the posterior in Equation 2.

$$L(\theta_{\text{obs}}|x) = \prod_{i=1}^{18} \frac{1}{\sigma_{\theta} \sqrt{2\pi}} \exp\left(-\frac{(\theta_{\text{obs},i} - \theta_{\text{cal},i})^2}{2\sigma_{\theta}^2}\right) \quad (1)$$

$$P(x|\theta_{\text{obs}}) = \frac{L(\theta_{\text{obs}}|x) \text{Prior}(x)}{\int dx L(\theta_{\text{obs}}|x) \text{Prior}(x)}. \quad (2)$$

But with 7 modules in each layer we have 14 dimensions, so a naive numerical integration will not work. We here use Monte Carlo integration, where each dimension has been sampled using a Gaussian.

To visualize the results, we marginalize all but the two coordinates of a module. Figure 5 shows the result from simulated data. The method can be applied with any number of measured angles and is robust to missing data, but for this test, only the cameras and LEDs of three modules were simulated. Table 1 presents the positional errors from the prior and posterior best-fit estimates. The posterior shows a clear improvement, with reduced distance errors indicating higher positional accuracy.

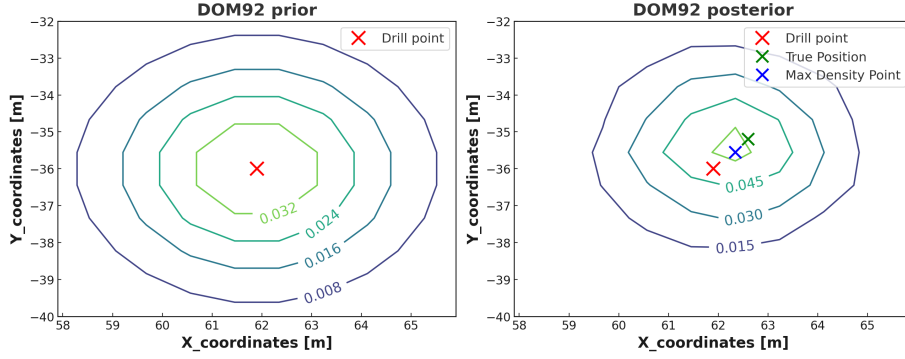


Figure 5: Contour plots of the prior (left) and posterior (right) probability distributions for DOM 92. The red cross indicates the drill point, the green cross the true position, and the blue cross the posterior best fit. The contours shrink and move closer to the true position, though some uncertainty remains due to Monte Carlo integration used in marginalization.

DOM	True Point (x, y)	Drill Point (x, y)	Prior Distance (m)	Best Fit Point (x, y)	Posterior Distance (m)
88	(47.3, -57.0)	(48.3, -56.5)	1.12	(47.0, -57.9)	0.95
92	(62.6, -35.2)	(61.9, -36.0)	1.06	(62.4, -35.3)	0.22
93	(27.0, -31.2)	(27.3, -30.5)	0.76	(27.0, -30.9)	0.30

Table 1: Comparison of initial and reconstructed positions for modules on strings 88, 92 and 93 and distances to true positions.

5. Conclusion and Outlook

We evaluated the performance and sensitivity of the IceCube Upgrade Camera System for its intended role within the IceCube Upgrade. The analysis used simulated images generated by the custom CamSim framework, which models image capture under various geometric configurations

and optical conditions. For geometry measurements, we showed that relative angles between DOMs, extracted from captured images, can be used within a Bayesian framework to reconstruct DOM positions with sub-meter precision. To study the ice's optical properties, we developed Transformer-based models trained on simulated images to infer the scattering length of the bulk ice and the bubble column, respectively. The models achieved high accuracy at a sub-percentage level.

The current model, trained on simulated images with varying scattering lengths, serves as a prototype for a more comprehensive framework. We aim to expand this approach by incorporating additional optical properties into the dataset, such as absorption length, scattering phase function, and anisotropy. This will enable the development of a unified model capable of inferring multiple ice properties from a single image. While the inclusion of correlated parameters may reduce sensitivity, it will lead to a more realistic and fully integrated model. To support this effort, future simulations will integrate a refined projection mechanism that accounts for photon propagation through the full optical path, including the pressure vessel, optical gel, mechanical mount, and lens. A water tank setup is currently being constructed at the University of Utah, where a real mDOM will be imaged under controlled conditions using a movable light source on an x–y gantry system.

References

- [1] **IceCube** Collaboration, *Nucl. Instr. Meth. Phys. Res. A* **601** no. 3, (2009) 294 – 316.
- [2] **IceCube** Collaboration, A. Ishihara, *PoS ICRC2019* (2021) 1031.
- [3] **IceCube** Collaboration, W. Kang, C. Tönnis, and C. Rott, *PoS ICRC2019* (2020) 928.
- [4] **IceCube** Collaboration, C. Hill, *PoS ICRC2021* (2021) 1042.
- [5] **IceCube** Collaboration, L. Classen, *PoS ICRC2021* (2021) 1070.
- [6] **IceCube** Collaboration, C. Rott and C. Tönnis, *PoS ICRC2023* (2023) 22.
- [7] **IceCube** Collaboration, D. Chirkin, *Nucl. Instrum. Meth. A* **725** (2013) 141–143.
- [8] A. Dosovitskiy, L. Beyer, A. Kolesnikov, D. Weissenborn, X. Zhai, T. Unterthiner, M. Dehghani, M. Minderer, G. Heigold, S. Gelly, J. Uszkoreit, and N. Houlsby, *arXiv preprint arXiv:2010.11929* (2021) .
- [9] A. Vaswani, N. Shazeer, N. Parmar, J. Uszkoreit, L. Jones, A. N. Gomez, Ł. Kaiser, and I. Polosukhin, “Attention is all you need,” in *Advances in Neural Information Processing Systems*, vol. 30, pp. 5998–6008. Curran Associates, Inc., 2017. [arXiv:1706.03762].
- [10] **IceCube** Collaboration, R. Abbasi *et al.*, *PoS ICRC2023* (2023) 988.
- [11] **IceCube** Collaboration, R. Abbasi *et al.*, *PoS ICRC2021* (2021) 1059.
- [12] **IceCube-Gen2** Collaboration, “IceCube-Gen2 Technical Design Report: part II,” in *IceCube-Gen2 Technical Design Report: part II*. 2023.
- [13] **IceCube** Collaboration, M. G. Aartsen *et al.*, *JINST* **12** no. 03, (2017) P03012.

Full Author List: IceCube Collaboration

R. Abbasi¹⁶, M. Ackermann⁶³, J. Adams¹⁷, S. K. Agarwalla^{39, a}, J. A. Aguilar¹⁰, M. Ahlers²¹, J.M. Alameddine²², S. Ali³⁵, N. M. Amin⁴³, K. Andeen⁴¹, C. Argüelles¹³, Y. Ashida⁵², S. Athanasiadou⁶³, S. N. Axani⁴³, R. Babu²³, X. Bai⁴⁹, J. Baines-Holmes³⁹, A. Balagopal V.^{39, 43}, S. W. Barwick²⁹, S. Bash²⁶, V. Basu⁵², R. Bay⁶, J. J. Beatty^{19, 20}, J. Becker Tjus^{9, b}, P. Behrens¹, J. Beise⁶¹, C. Bellenghi²⁶, B. Benkel⁶³, S. BenZvi⁵¹, D. Berley¹⁸, E. Bernardini^{47, c}, D. Z. Besson³⁵, E. Blaufuss¹⁸, L. Bloom⁵⁸, S. Blot⁶³, I. Bodo³⁹, F. Bontempo³⁰, J. Y. Book Motzkin¹³, C. Boscolo Meneguolo^{47, c}, S. Böser⁴⁰, O. Botner⁶¹, J. Böttcher¹, J. Braun³⁹, B. Brinson⁴, Z. Brisson-Tsavoussis³², R. T. Burley², D. Butterfield³⁹, M. A. Campana⁴⁸, K. Carloni¹³, J. Carpio^{33, 34}, S. Chattopadhyay^{39, a}, N. Chau¹⁰, Z. Chen⁵⁵, D. Chirkin³⁹, S. Choi⁵², B. A. Clark¹⁸, A. Coleman⁶¹, P. Coleman¹, G. H. Collin¹⁴, D. A. Coloma Borja⁴⁷, A. Connolly^{19, 20}, J. M. Conrad¹⁴, R. Corley⁵², D. F. Cowen^{59, 60}, C. De Clercq¹¹, J. J. DeLaunay⁵⁹, D. Delgado¹³, T. Delmeulle¹⁰, S. Deng¹, P. Desiati³⁹, K. D. de Vries¹¹, G. de Wasseige³⁶, T. DeYoung²³, J. C. Díaz-Vélez³⁹, S. DiKerby²³, M. Dittmer⁴², A. Domi²⁵, L. Draper⁵², L. Dueser¹, D. Durnford²⁴, K. Dutta⁴⁰, M. A. DuVernois³⁹, T. Ehrhardt⁴⁰, L. Eidenschink²⁶, A. Eimer²⁵, P. Eller²⁶, E. Ellinger⁶², D. Elsässer²², R. Engel^{30, 31}, H. Erpenbeck³⁹, W. Esmail⁴², S. Eulig¹³, J. Evans¹⁸, P. A. Evenson⁴³, K. L. Fan¹⁸, K. Fang³⁹, K. Farrag¹⁵, A. R. Fazely⁵, A. Fedynitch⁵⁷, N. Feigl⁸, C. Finley⁵⁴, L. Fischer⁶³, D. Fox⁵⁹, A. Franckowiak⁹, S. Fukami⁶³, P. Fürst¹, J. Gallagher³⁸, E. Ganster¹, A. Garcia¹³, M. Garcia⁴³, G. Garg^{39, a}, E. Genton^{13, 36}, L. Gerhardt⁷, A. Ghadimi⁵⁸, C. Glaser⁶¹, T. Glüsenkamp⁶¹, J. G. Gonzalez⁴³, S. Goswami^{33, 34}, A. Granados²³, D. Grant¹², S. J. Gray¹⁸, S. Griffin³⁹, S. Griswold⁵¹, K. M. Groth²¹, D. Guevel³⁹, C. Günther¹, P. Gutjahr²², C. Ha⁵³, C. Haack²⁵, A. Hallgren⁶¹, L. Halve¹, F. Halzen³⁹, L. Hamacher¹, M. Ha Minh²⁶, M. Handt¹, K. Hanson³⁹, J. Hardin¹⁴, A. A. Harnisch²³, P. Hatch³², A. Haungs³⁰, J. Häußler¹, K. Helbing⁶², J. Hellrung⁹, B. Henke²³, L. Hennig²⁵, F. Henningsen¹², L. Heuermann¹, R. Hewett¹⁷, N. Heyer⁶¹, S. Hickford⁶², A. Hidvegi⁵⁴, C. Hill¹⁵, G. C. Hill², R. Hmaid¹⁵, K. D. Hoffman¹⁸, D. Hooper³⁹, S. Hori³⁹, K. Hoshina^{39, d}, M. Hostert¹³, W. Hou³⁰, T. Huber³⁰, K. Hultqvist⁵⁴, K. Hymon^{22, 57}, A. Ishihara¹⁵, W. Iwakiri¹⁵, M. Jacquart²¹, S. Jain³⁹, O. Janik²⁵, M. Jansson³⁶, M. Jeong⁵², M. Jin¹³, N. Kamp¹³, D. Kang³⁰, W. Kang⁴⁸, X. Kang⁴⁸, A. Kappes⁴², L. Kardum²², T. Karg⁶³, M. Karl²⁶, A. Karle³⁹, A. Katil²⁴, M. Kauer³⁹, J. L. Kelley³⁹, M. Khanal⁵², A. Khatee Zathul³⁹, A. Kheirandish^{33, 34}, H. Kimku⁵³, J. Kiryluk⁵⁵, C. Klein²⁵, S. R. Klein^{6, 7}, Y. Kobayashi¹⁵, A. Kochocki²³, R. Koirala⁴³, H. Kolanoski⁸, T. Kontrimas²⁶, L. Köpke⁴⁰, C. Kopper²⁵, D. J. Koskinen²¹, P. Koundal⁴³, M. Kowalski^{8, 63}, T. Kozynets²¹, N. Krieger⁹, J. Krishnamoorthi^{39, a}, T. Krishnan¹³, K. Kruiswijk³⁶, E. Krupczak²³, A. Kumar⁶³, E. Kun⁹, N. Kurahashi⁴⁸, N. Lad⁶³, C. Lagunas Gualda²⁶, L. Lallement Arnaud¹⁰, M. Lamoureux³⁶, M. J. Larson¹⁸, F. Lauber⁶², J. P. Lazar³⁶, K. Leonard DeHolton⁶⁰, A. Leszczyńska⁴³, J. Liao⁴, C. Lin⁴³, Y. T. Liu⁶⁰, M. Liubarska²⁴, C. Love⁴⁸, L. Lu³⁹, F. Lucarelli²⁷, W. Luszczyk^{19, 20}, Y. Lyu^{6, 7}, J. Madsen³⁹, E. Magnus¹¹, K. B. M. Mahn²³, Y. Makino³⁹, E. Manao²⁶, S. Mancina^{47, e}, A. Mand³⁹, I. C. Mariş¹⁰, S. Marka⁴⁵, Z. Marka⁴⁵, L. Marten¹, I. Martinez-Soler¹³, R. Maruyama⁴⁴, J. Mauro³⁶, F. Mayhew²³, F. McNally³⁷, J. V. Mead²¹, K. Meagher³⁹, S. Mechbal⁶³, A. Medina²⁰, M. Meier¹⁵, Y. Merckx¹¹, L. Merten⁹, J. Mitchell⁵, L. Molchany⁴⁹, T. Montaruli²⁷, R. W. Moore²⁴, Y. Morii¹⁵, A. Mosbrugger²⁵, M. Moulai³⁹, D. Mousadi⁶³, E. Moyaux³⁶, T. Mukherjee³⁰, R. Naab⁶³, M. Nakos³⁹, U. Naumann⁶², J. Necker⁶³, L. Neste⁵⁴, M. Neumann⁴², H. Niederhausen²³, M. U. Nisa²³, K. Noda¹⁵, A. Noell¹, A. Novikov⁴³, A. Obertacke Pollmann¹⁵, V. O'Dell³⁹, A. Olivas¹⁸, R. Orsoe²⁶, J. Osborn³⁹, E. O'Sullivan⁶¹, V. Palusova⁴⁰, H. Pandya⁴³, A. Parenti¹⁰, N. Park³², V. Parrish²³, E. N. Paudel⁵⁸, L. Paul⁴⁹, C. Pérez de los Heros⁶¹, T. Pernice⁶³, J. Peterson³⁹, M. Plum⁴⁹, A. Pontén⁶¹, V. Poojyam⁵⁸, Y. Popovych⁴⁰, M. Prado Rodriguez³⁹, B. Pries²³, R. Procter-Murphy¹⁸, G. T. Przybylski⁷, L. Pyras⁵², C. Raab³⁶, J. Rack-Helleis⁴⁰, N. Rad⁶³, M. Ravn⁶¹, K. Rawlins³, Z. Rechav³⁹, A. Rehman³⁹, I. Reistoffer⁴⁹, E. Resconi²⁶, S. Reusch⁶³, C. D. Rho⁵⁶, W. Rhode²², L. Ricca³⁶, B. Riedel³⁹, A. Rifaie⁶², E. J. Roberts², S. Robertson^{6, 7}, M. Rongen²⁵, A. Rosted¹⁵, C. Rott⁵², T. Ruhe²², L. Ruohan²⁶, D. Ryckbosch²⁸, J. Saffer³¹, D. Salazar-Gallegos²³, P. Sampathkumar³⁰, A. Sandrock⁶², G. Sanger-Johnson²³, M. Santander⁵⁸, S. Sarkar⁴⁶, J. Savelberg¹, M. Scarnera³⁶, P. Schaile²⁶, M. Schaufel¹, H. Schieler³⁰, S. Schindler²⁵, L. Schlickmann⁴⁰, B. Schlüter⁴², F. Schlüter¹⁰, N. Schmeisser⁶², T. Schmidt¹⁸, F. G. Schröder^{30, 43}, L. Schumacher²⁵, S. Schwirn¹, S. Sclafani¹⁸, D. Seckel⁴³, L. Seen³⁹, M. Seikh³⁵, S. Seunarine⁵⁰, P. A. Seyle Myhr³⁶, R. Shah⁴⁸, S. Shefali³¹, N. Shimizu¹⁵, B. Skrzypek⁶, R. Snihur³⁹, J. Soedingrekso²², A. Sogaard²¹, D. Soldin⁵², P. Soldin¹, G. Sommani⁹, C. Spannfellner²⁶, G. M. Spiczak⁵⁰, C. Spiering⁶³, J. Stachurska²⁸, M. Stamatikos²⁰, T. Stanev⁴³, T. Stezelberger⁷, T. Stürwald⁶², T. Stuttgart²¹, G. W. Sullivan¹⁸, I. Taboada⁴, S. Ter-Antonyan⁵, A. Terliuk²⁶, A. Thakuri⁴⁹, M. Thiesmeyer³⁹, W. G. Thompson¹³, J. Thwaites³⁹, S. Tilav⁴³, K. Tollefson²³, S. Toscano¹⁰, D. Tosi³⁹, A. Trettin⁶³, A. K. Upadhyay^{39, a}, K. Upshaw⁵, A. Vaidyanathan⁴¹, N. Valtonen-Mattila^{9, 61}, J. Valverde⁴¹, J. Vandenbroucke³⁹, T. van Eeden⁶³, N. van Eijndhoven¹¹, L. van Rootselaar²², J. van Santen⁶³, F. J. Vara Carbonell⁴², F. Varsi³¹, M. Venugopal³⁰, M. Vereecken³⁶, S. Vergara Carrasco¹⁷, S. Verpoest⁴³, D. Veske⁴⁵, A. Vijai¹⁸, J. Villarreal¹⁴, C. Walck⁵⁴, A. Wang⁴, E. Warrick⁵⁸, C. Weaver²³, P. Weigel¹⁴, A. Weindl³⁰, J. Weldert⁴⁰, A. Y. Wen¹³, C. Wendt³⁹, J. Werthebach²², M. Weyrauch³⁰, N. Whitehorn²³, C. H. Wiebusch¹, D. R. Williams⁵⁸, L. Witthaus²², M. Wolf²⁶, G. Wrede²⁵, X. W. Xu⁵, J. P. Yañez²⁴, Y. Yao³⁹, E. Yildizci³⁹, S. Yoshida¹⁵, R. Young³⁵, F. Yu¹³, S. Yu⁵², T. Yuan³⁹, A. Zegarelli⁹, S. Zhang²³, Z. Zhang⁵⁵, P. Zhelnin¹³, P. Zilberman³⁹

¹ III. Physikalisches Institut, RWTH Aachen University, D-52056 Aachen, Germany² Department of Physics, University of Adelaide, Adelaide, 5005, Australia³ Dept. of Physics and Astronomy, University of Alaska Anchorage, 3211 Providence Dr., Anchorage, AK 99508, USA⁴ School of Physics and Center for Relativistic Astrophysics, Georgia Institute of Technology, Atlanta, GA 30332, USA⁵ Dept. of Physics, Southern University, Baton Rouge, LA 70813, USA⁶ Dept. of Physics, University of California, Berkeley, CA 94720, USA⁷ Lawrence Berkeley National Laboratory, Berkeley, CA 94720, USA⁸ Institut für Physik, Humboldt-Universität zu Berlin, D-12489 Berlin, Germany⁹ Fakultät für Physik & Astronomie, Ruhr-Universität Bochum, D-44780 Bochum, Germany¹⁰ Université Libre de Bruxelles, Science Faculty CP230, B-1050 Brussels, Belgium

- ¹¹ Vrije Universiteit Brussel (VUB), Dienst ELEM, B-1050 Brussels, Belgium
- ¹² Dept. of Physics, Simon Fraser University, Burnaby, BC V5A 1S6, Canada
- ¹³ Department of Physics and Laboratory for Particle Physics and Cosmology, Harvard University, Cambridge, MA 02138, USA
- ¹⁴ Dept. of Physics, Massachusetts Institute of Technology, Cambridge, MA 02139, USA
- ¹⁵ Dept. of Physics and The International Center for Hadron Astrophysics, Chiba University, Chiba 263-8522, Japan
- ¹⁶ Department of Physics, Loyola University Chicago, Chicago, IL 60660, USA
- ¹⁷ Dept. of Physics and Astronomy, University of Canterbury, Private Bag 4800, Christchurch, New Zealand
- ¹⁸ Dept. of Physics, University of Maryland, College Park, MD 20742, USA
- ¹⁹ Dept. of Astronomy, Ohio State University, Columbus, OH 43210, USA
- ²⁰ Dept. of Physics and Center for Cosmology and Astro-Particle Physics, Ohio State University, Columbus, OH 43210, USA
- ²¹ Niels Bohr Institute, University of Copenhagen, DK-2100 Copenhagen, Denmark
- ²² Dept. of Physics, TU Dortmund University, D-44221 Dortmund, Germany
- ²³ Dept. of Physics and Astronomy, Michigan State University, East Lansing, MI 48824, USA
- ²⁴ Dept. of Physics, University of Alberta, Edmonton, Alberta, T6G 2E1, Canada
- ²⁵ Erlangen Centre for Astroparticle Physics, Friedrich-Alexander-Universität Erlangen-Nürnberg, D-91058 Erlangen, Germany
- ²⁶ Physik-department, Technische Universität München, D-85748 Garching, Germany
- ²⁷ Département de physique nucléaire et corpusculaire, Université de Genève, CH-1211 Genève, Switzerland
- ²⁸ Dept. of Physics and Astronomy, University of Gent, B-9000 Gent, Belgium
- ²⁹ Dept. of Physics and Astronomy, University of California, Irvine, CA 92697, USA
- ³⁰ Karlsruhe Institute of Technology, Institute for Astroparticle Physics, D-76021 Karlsruhe, Germany
- ³¹ Karlsruhe Institute of Technology, Institute of Experimental Particle Physics, D-76021 Karlsruhe, Germany
- ³² Dept. of Physics, Engineering Physics, and Astronomy, Queen's University, Kingston, ON K7L 3N6, Canada
- ³³ Department of Physics & Astronomy, University of Nevada, Las Vegas, NV 89154, USA
- ³⁴ Nevada Center for Astrophysics, University of Nevada, Las Vegas, NV 89154, USA
- ³⁵ Dept. of Physics and Astronomy, University of Kansas, Lawrence, KS 66045, USA
- ³⁶ Centre for Cosmology, Particle Physics and Phenomenology - CP3, Université catholique de Louvain, Louvain-la-Neuve, Belgium
- ³⁷ Department of Physics, Mercer University, Macon, GA 31207-0001, USA
- ³⁸ Dept. of Astronomy, University of Wisconsin—Madison, Madison, WI 53706, USA
- ³⁹ Dept. of Physics and Wisconsin IceCube Particle Astrophysics Center, University of Wisconsin—Madison, Madison, WI 53706, USA
- ⁴⁰ Institute of Physics, University of Mainz, Staudinger Weg 7, D-55099 Mainz, Germany
- ⁴¹ Department of Physics, Marquette University, Milwaukee, WI 53201, USA
- ⁴² Institut für Kernphysik, Universität Münster, D-48149 Münster, Germany
- ⁴³ Bartol Research Institute and Dept. of Physics and Astronomy, University of Delaware, Newark, DE 19716, USA
- ⁴⁴ Dept. of Physics, Yale University, New Haven, CT 06520, USA
- ⁴⁵ Columbia Astrophysics and Nevis Laboratories, Columbia University, New York, NY 10027, USA
- ⁴⁶ Dept. of Physics, University of Oxford, Parks Road, Oxford OX1 3PU, United Kingdom
- ⁴⁷ Dipartimento di Fisica e Astronomia Galileo Galilei, Università Degli Studi di Padova, I-35122 Padova PD, Italy
- ⁴⁸ Dept. of Physics, Drexel University, 3141 Chestnut Street, Philadelphia, PA 19104, USA
- ⁴⁹ Physics Department, South Dakota School of Mines and Technology, Rapid City, SD 57701, USA
- ⁵⁰ Dept. of Physics, University of Wisconsin, River Falls, WI 54022, USA
- ⁵¹ Dept. of Physics and Astronomy, University of Rochester, Rochester, NY 14627, USA
- ⁵² Department of Physics and Astronomy, University of Utah, Salt Lake City, UT 84112, USA
- ⁵³ Dept. of Physics, Chung-Ang University, Seoul 06974, Republic of Korea
- ⁵⁴ Oskar Klein Centre and Dept. of Physics, Stockholm University, SE-10691 Stockholm, Sweden
- ⁵⁵ Dept. of Physics and Astronomy, Stony Brook University, Stony Brook, NY 11794-3800, USA
- ⁵⁶ Dept. of Physics, Sungkyunkwan University, Suwon 16419, Republic of Korea
- ⁵⁷ Institute of Physics, Academia Sinica, Taipei, 11529, Taiwan
- ⁵⁸ Dept. of Physics and Astronomy, University of Alabama, Tuscaloosa, AL 35487, USA
- ⁵⁹ Dept. of Astronomy and Astrophysics, Pennsylvania State University, University Park, PA 16802, USA
- ⁶⁰ Dept. of Physics, Pennsylvania State University, University Park, PA 16802, USA
- ⁶¹ Dept. of Physics and Astronomy, Uppsala University, Box 516, SE-75120 Uppsala, Sweden
- ⁶² Dept. of Physics, University of Wuppertal, D-42119 Wuppertal, Germany
- ⁶³ Deutsches Elektronen-Synchrotron DESY, Platanenallee 6, D-15738 Zeuthen, Germany
- ^a also at Institute of Physics, Sachivalaya Marg, Sainik School Post, Bhubaneswar 751005, India
- ^b also at Department of Space, Earth and Environment, Chalmers University of Technology, 412 96 Gothenburg, Sweden
- ^c also at INFN Padova, I-35131 Padova, Italy
- ^d also at Earthquake Research Institute, University of Tokyo, Bunkyo, Tokyo 113-0032, Japan
- ^e now at INFN Padova, I-35131 Padova, Italy

Acknowledgments

The authors gratefully acknowledge the support from the following agencies and institutions: USA – U.S. National Science Foundation-Office of Polar Programs, U.S. National Science Foundation-Physics Division, U.S. National Science Foundation-EPSCoR, U.S. National Science Foundation-Office of Advanced Cyberinfrastructure, Wisconsin Alumni Research Foundation, Center for High Throughput Computing (CHTC) at the University of Wisconsin–Madison, Open Science Grid (OSG), Partnership to Advance Throughput Computing (PATH), Advanced Cyberinfrastructure Coordination Ecosystem: Services & Support (ACCESS), Frontera and Ranch computing project at the Texas Advanced Computing Center, U.S. Department of Energy-National Energy Research Scientific Computing Center, Particle astrophysics research computing center at the University of Maryland, Institute for Cyber-Enabled Research at Michigan State University, Astroparticle physics computational facility at Marquette University, NVIDIA Corporation, and Google Cloud Platform; Belgium – Funds for Scientific Research (FRS-FNRS and FWO), FWO Odysseus and Big Science programmes, and Belgian Federal Science Policy Office (Belspo); Germany – Bundesministerium für Forschung, Technologie und Raumfahrt (BMFTR), Deutsche Forschungsgemeinschaft (DFG), Helmholtz Alliance for Astroparticle Physics (HAP), Initiative and Networking Fund of the Helmholtz Association, Deutsches Elektronen Synchrotron (DESY), and High Performance Computing cluster of the RWTH Aachen; Sweden – Swedish Research Council, Swedish Polar Research Secretariat, Swedish National Infrastructure for Computing (SNIC), and Knut and Alice Wallenberg Foundation; European Union – EGI Advanced Computing for research; Australia – Australian Research Council; Canada – Natural Sciences and Engineering Research Council of Canada, Calcul Québec, Compute Ontario, Canada Foundation for Innovation, WestGrid, and Digital Research Alliance of Canada; Denmark – Villum Fonden, Carlsberg Foundation, and European Commission; New Zealand – Marsden Fund; Japan – Japan Society for Promotion of Science (JSPS) and Institute for Global Prominent Research (IGPR) of Chiba University; Korea – National Research Foundation of Korea (NRF); Switzerland – Swiss National Science Foundation (SNSF).